Phase binarization in mutually synchronized bias field free spin-Hall nano-oscillators for reservoir computing

Sourabh Manna [1], Rohit Medwal [2], John Rex Mohan [3], Yasuhiro Fukuma [3,4] and Rajdeep Singh Rawat [1,*]

[1] *Natural Sciences and Science Education, National Institute of Education, Nanyang Technological University 637616, Singapore*
[2] *Department of Physics, Indian Institute of Technology Kanpur, Uttar Pradesh 208016, India*
[3] *Faculty of Computer Science and System Engineering, Kyushu Institute of Technology, Iizuka 820-8502, Japan*
[4] *Research Center for Neuromorphic AI hardware, Kyushu Institute of Technology, Kitakyushu 808-0196, Japan*

(Received 2 April 2024; accepted 24 May 2024; published 18 June 2024)

Mutually coupled spin-Hall nano-oscillators (SHNO) can exhibit a binarized phase state, offering pathways to realize Ising machines and efficient neuromorphic hardware. Conventionally, phase binarization is achieved in coupled identical SHNOs via injecting an external microwave at twice the oscillator frequency in the presence of a strong biasing magnetic field. However, this technology poses potential challenges of higher energy consumption and complex circuit design. Moreover, differences in the individual characteristic frequencies of SHNOs resulting from fabrication-induced mismatch in SHNO dimensions may hinder their mutual synchronization. Addressing these challenges, we demonstrate purely dc current-driven mutual synchronization and phase binarization of two nonidentical nanoconstriction SHNOs without biasing magnetic field and microwave injection. We thoroughly investigate these phenomena and underlying mechanisms using micromagnetic simulation. We show how the localized fundamental mode of the spin wave emerging from the magnetization auto-oscillation reinforces the mutual synchronization, while the second-harmonic spin wave induces the phase binarization in the coupled SHNO pair. We further demonstrate the bias field free synchronized SHNO pair efficiently performing a reservoir computing benchmark learning task: sin- and square-wave classification, with 100% accuracy, utilizing the current-tunable phase binarization phenomenon. Our results showcase promising magnetization dynamics of coupled bias field free SHNOs for future computing applications.

DOI: 10.1103/PhysRevB.109.214425

I. INTRODUCTION

Reservoir computing [1,2] (RC) is a promising computing paradigm that harnesses the nonlinear dynamics of complex systems for efficient information processing. RC comprises a time-dependent recurrent neural network known as the "reservoir" and a time-invariant "readout" that connects the reservoir to the output. Unlike traditional neural networks, only the readout is trained in RC using linear regression that significantly reduces the training cost [3]. On-chip RC hardware can be designed by exploiting the rich nonlinear dynamics of coupled nano-oscillators [4,5]. Parametrically driven oscillator networks are already established to implement phase-logic operation via subharmonic injection-locking (SHIL) method in Boolean computing [6–8]. In such oscillators, two possible phase states are observed (phase binarization) which represent the binary "0" and "1" in phase logic. This phase binarization can modulate the coupling between the oscillators and enhance the nonlinearity in the dynamic variables [9]. Therefore, phase-binarized coupled nano-oscillators hold significant potential for RC hardware implementation.

Recently, ferromagnet (FM)/heavy-metal bilayer-based spin Hall nano-oscillators (SHNO) have emerged as one of the top-tier complementary metal-oxide semiconductor compatible high-frequency nano-oscillators [10] for realizing RC hardware, owing to their inherent nonlinear magnetization dynamics [11–14], miniature footprint [14–16], straightforward fabrication, and low-power operation [17]. Additionally, efficient control of magnetization dynamics through bias-current, magnetic field, voltage-controlled magnetic anisotropy, and microwave injection locking makes them suitable for neuromorphic hardware design [13,16,18–23]. Multiple nanoconstriction (NC) SHNOs can be mutually coupled through propagating spin wave, exchange interaction, and magnetodipolar interaction, eliminating the need for electrical interconnects in SHNO arrays [24–28]. The current state of the art demonstrates SHIL-induced phase binarization in a two-dimensional NC SHNO array where the inter-SHNO coupling is primarily mediated by magnetodipolar interaction [29], paving a way towards realizing spin-Hall Ising machine for efficiently solving computationally hard combinatorial optimization problems. Therefore, phase binarization in mutually coupled SHNOs can be a promising way for designing RC hardware as well. Nevertheless, practical implementation of this route poses major challenges. The reliance on external biasing magnetic field for typical SHNO operation and external microwave source for implementation of SHIL lead to complexity in circuit design process, increased circuit area, and higher energy consumption. Hence, exploring phase binarization routes that exploit intrinsic

*Contact author: rajdeep.rawat@nie.edu.sg

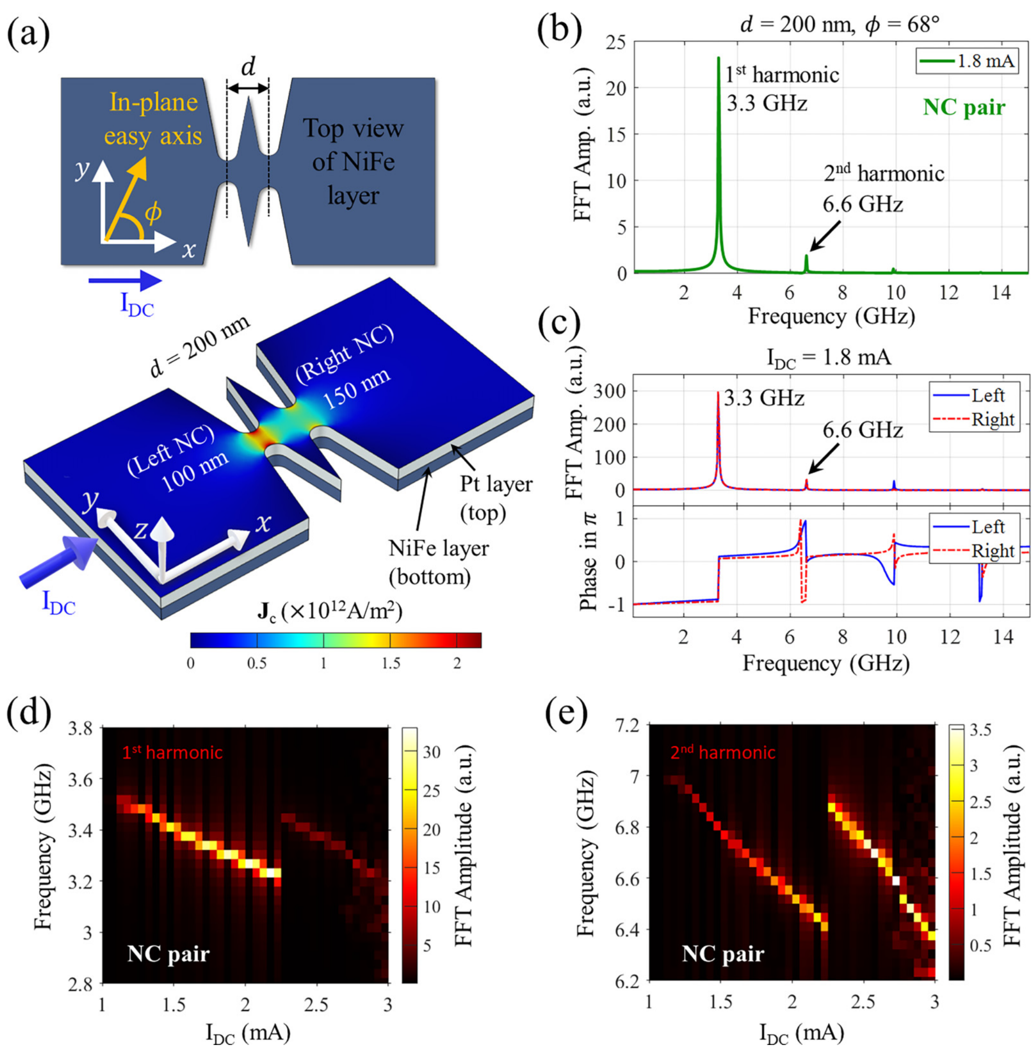

FIG. 1. Schematic of the device geometry and auto-oscillation characteristics. (a) The NC pair geometry designed in COMSOL and the spatial distribution of current density in the Pt layer. (b) FFT spectrum of the auto-oscillation obtained from the entire NC pair geometry for $I_{dc} = 1.8$ mA. (c) FFT spectra of the local auto-oscillation at individual NCs in the NC pair. (d) Current tunability of the first harmonic of auto-oscillation in the NC pair. (e) Current tunability of the second harmonic of the auto-oscillation in the NC pair.

magnetization dynamics in coupled SHNOs systems without external biasing magnetic field or microwave sources is imperative.

Recent studies on bias field free single SHNO have demonstrated nontrivial auto-oscillation properties including in-plane to out-of-plane transition of auto-oscillation trajectory [30–32], reduction of threshold current [33], and tunable spiking behavior [31,34]. Investigating mutual synchronization of bias field free NC SHNOs, therefore, can unveil intriguing magnetization dynamics for realization of efficient RC hardware. However, challenges arise due to fabrication-induced mismatch in nanoconstriction widths causing a difference in characteristic frequencies of individual SHNOs in an NC array. This frequency mismatch is detrimental for their mutual synchronization. This issue can be resolved by introducing a gradient in the biasing magnetic field [26] which is technically not allowed for bias field free SHNOs. Therefore, exploring routes for mutual synchronization of bias field free SHNOs with nonidentical NC widths is crucial for practical applications.

In this paper we demonstrate purely dc current-driven phase binarization in a mutually synchronized NC SHNO pair without any biasing magnetic field, as well as external microwave injection. The SHNO pair is designed by defining two NCs with nonidentical widths, representing two different SHNOs separated by a distance (d) as shown in Fig. 1(a). We comprehensively investigate the mechanism of mutual synchronization and dc current-driven phase binarization in bias field free condition. More importantly, we demonstrate that the phase-binarized bias field free SHNO pair can efficiently perform an RC benchmark learning task: sin- and square-wave classification.

In our previous work, we demonstrated that an in-plane uniaxial anisotropy can induce bias field free auto-oscillation of magnetization in a NiFe/Pt bilayer-based NC SHNO device [33]. Such a magnetic anisotropy can be induced in NiFe by implementing suitable growth schemes [35–38]. Hence, we chose a similar NiFe/Pt bilayer-based NC pair as shown in Fig. 1(a). We defined the in-plane uniaxial anisotropy in the NiFe layer with the easy axis oriented at an angle ϕ measured from the x axis [Fig. 1(a)]. The uniaxial anisotropy gives rise to the anisotropy field given as $\boldsymbol{H}_{\text{anis}} = \frac{2K_u}{M_s}(\hat{\boldsymbol{u}} \cdot \boldsymbol{m})\hat{\boldsymbol{u}}$, where K_u, M_s, $\boldsymbol{m}$, and $\hat{\boldsymbol{u}}$ are the uniaxial anisotropy constant, saturation magnetization of NiFe, reduced magnetization vector ($\boldsymbol{m} = \boldsymbol{M}/M_s$), and the unit vector along the easy axis, respectively. In the stable equilibrium, the orientation of magnetization is determined by the cumulative effect of magnetic anisotropy, magnetostatic field, and exchange interaction. As we pass a charge current through the SHNO device, it induces a transverse spin current via spin-Hall effect in Pt. The spin current exerts spin-orbit torque (SOT) on the magnetization in NiFe and destabilizes it from the stable equilibrium. The SOT may enhance or oppose the intrinsic damping torque in the ferromagnet based on the mutual orientation of the magnetization and the spin polarization ($\boldsymbol{\sigma}$) of the injected spin current. In the latter case, a large enough SOT can completely compensate for the intrinsic damping torque and lead to the limit-cycle auto-oscillation of magnetization about the effective internal field ($\boldsymbol{H}_{\text{eff}}$). In the absence of any biasing magnetic field, $\boldsymbol{H}_{\text{eff}}$ is given as

$$\boldsymbol{H}_{\text{eff}} = \boldsymbol{H}_{\text{anis}} + \boldsymbol{H}_{\text{demag}} + \boldsymbol{H}_{\text{exch}} + \boldsymbol{H}_{Oe}, \tag{1}$$

where $\boldsymbol{H}_{\text{demag}}$, $\boldsymbol{H}_{\text{exch}}$, and $\boldsymbol{H}_{Oe}$ denote the magnetostatic field, the exchange field, and the dc current-induced Oersted field, respectively. The SOT-driven magnetization dynamics can be quantitatively formulated in terms of the Landau-Lifshitz-Gilbert (LLG) equation with additional SOT term as follows [39,40]:

$$\dot{\boldsymbol{m}} = -\gamma \boldsymbol{m} \times \boldsymbol{H}_{\text{eff}} + \alpha \boldsymbol{m} \times \dot{\boldsymbol{m}} + \frac{\gamma |\boldsymbol{J}_c| \hbar \theta_{SH}}{2 e t_{FM} \mu_0 M_s} \boldsymbol{m} \times (\boldsymbol{\sigma} \times \boldsymbol{m}). \tag{2}$$

In Eq. (2), α denotes the intrinsic damping parameter, and θ_{SH} is the spin-Hall angle of Pt, which is taken as 0.08 [19,24,25] in the present study. The quantities in the SOT term, γ, $\hbar$, e, μ_0, $\boldsymbol{\sigma}$, and t_{FM}, represent the gyromagnetic ratio, reduced Planck's constant, electronic charge, permeability of vacuum, spin-polarization direction, and thickness of the NiFe layer, respectively. Notably, the fieldlike component of SOT arising from the bulk of Pt and interfacial Rashba effect has been found to be significantly smaller than the dampinglike component of SOT in NiFe/Pt system [40,41]. Therefore, the SOT-driven magnetization dynamics in such system is efficiently modeled considering only the dampinglike component of SOT. We have employed the micromagnetic modeling approach to numerically solve Eq. (2) (see the Appendix) and obtained the oscillatory magnetization dynamics in bias field free condition.

II. RESULTS

A. Device design and auto-oscillation properties

We consider an NC SHNO pair consisting of a 5-nm-thick NiFe layer possessing uniaxial anisotropy, interfaced with a 5-nm-thick Pt layer [Fig. 1(a)]. The two NCs of widths 100 nm (left NC) and 150 nm (right NC) are separated by a center-to-center distance, $d = 200$ nm. From here on, we will refer to this NC SHNO pair as "NC pair." Figure 1(a) schematically represents the device structure of the NC pair and the spatial distribution of current density ($\boldsymbol{J}_c$) in the Pt layer for 1 mA input current (I_{dc}), as obtained from Multiphysics simulation using COMSOL (see the Appendix). We explicitly consider the dominant x component of $\boldsymbol{J}_c$ for computing the current-induced spin-orbit torque as the y and z components are an order of magnitude smaller than the x component (see Supplemental Material [42], Fig. S1). Therefore, we defined $\boldsymbol{\sigma} = -\hat{\boldsymbol{y}}$ considering the orthogonality of $\boldsymbol{J}_c$, $\boldsymbol{\sigma}$, and the spin current ($\boldsymbol{J}_s$) along $-\hat{\boldsymbol{z}}$. As obvious from Fig. 1(a), $\boldsymbol{J}_c$ at the left NC is higher as compared to the right NC. This essentially leads to lower threshold current for auto-oscillation in the left NC.

We numerically solved Eq. (2) using the GPU-accelerated micromagnetic solver MUMAX3 [43] to obtain the SOT-driven magnetization dynamics in the NC pair (see the Appendix for details of micromagnetic simulation). We explicitly defined $K_u = 7.5$ kJ/m^3 to account for the uniaxial anisotropy [33]. This induces an anisotropy field of 25 mT. The solver computes m_x as a function of time (t) at each micromagnetic cell. In the auto-oscillation state, the frequency of limit-cycle oscillation has been extracted by performing fast Fourier transform (FFT) of the spatial average of $m_x(t)$ obtained from the entire geometry. In experiments, the oscillation of $m_x(t)$ gives rise to oscillating anisotropic magnetoresistance (AMR), which is coupled with I_{dc} and subsequently converted into a longitudinal microwave voltage across the SHNO. The $m_y(t)$ and $m_z(t)$ are not associated with this AMR-based detection technique. Therefore, we analyze the $m_x(t)$ to find the auto-oscillation characteristics.

A typical FFT spectrum corresponding to the limit-cycle auto-oscillation for $I_{dc} = 1.8$ mA is shown in Fig. 1(b). The sharp peak at 3.3 GHz is accompanied by a weak second harmonic of 6.6 GHz. We further obtained the local auto-oscillation characteristics of individual NC SHNO within the NC pair by averaging $m_x(t)$ over 170 nm×170 nm area around the center of each NC and applying FFT. Figure 1(c) shows the frequency and phase extracted from the FFT of the local magnetization auto-oscillation profile in individual NCs. It is clear from Fig. 1(c) that both SHNOs in the NC pair exhibit the same auto-oscillation frequency and phase at 1.8 mA current, denoting mutual synchronization. Therefore, the auto-oscillation frequency of individual NC SHNOs [Fig. 1(c)] matches with the auto-oscillation frequency of the entire NC pair [Fig. 1(b)]. We further observe the current tunability of the auto-oscillation frequency and amplitude, obtained from the entire NC pair for both first harmonic [Fig. 1(d)] and second harmonic [Fig. 1(e)]. The redshift behavior of the frequency as a function of I_{dc} is consistent with our previous study on bias field free single-NC SHNO [33]. We notice from Figs. 1(d) and 1(e) that despite the difference in the NC widths, the NC pair exhibits auto-oscillation synchronously for each I_{dc} value at first harmonic as well as second harmonic. This persistent mutual synchronization of both NC SHNOs for more than 1.5 mA span of I_{dc} is comparable with the state-of-the-art in-plane field-assisted SHNO pair [25]. For both harmonics, the NC array exhibits redshift in auto-oscillation with increase in FFT amplitude for I_{dc} from about 1.1 to 2.2 mA. A sudden nonlinear blueshift is observed around 2.2 mA for both harmonics, which is explained later. For $I_{dc} \geqslant 2.25$ mA, both harmonics show the redshift again with increasing I_{dc}. However, while the FFT amplitude of

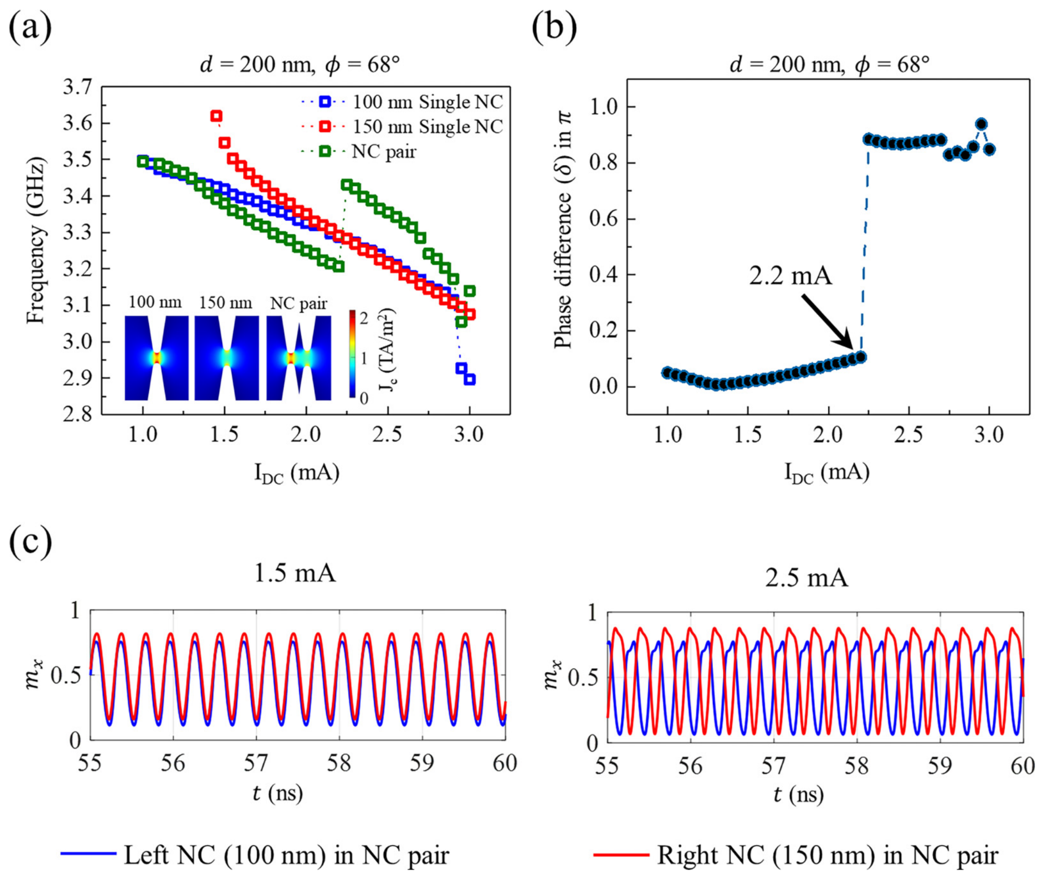

FIG. 2. Mutual synchronization of NC SHNOs and phase binarization. (a) Comparison of the current tunability of auto-oscillation frequency in the NC pair at mutually synchronized state, with the single NC SHNOs. The inset shows the current-density distribution at the vicinity of the NCs in single-NC SHNO and NC pair. (b) Phase difference for the first harmonic between the two NC SHNOs in the NC pair as a function of I_{dc}. The phase binarization threshold current 2.2 mA has been denoted by the pair. (c) Temporal profile of the local magnetization auto-oscillation in the individual NCs for input current of 1.5 mA (in-phase auto-oscillation) and 2.5 mA (out-of-phase auto-oscillation).

first harmonic decreases significantly in this I_{dc} regime, the amplitude of second harmonic continues to increase.

To gain a deeper insight into the mutual synchronization phenomenon, we separately simulated and analyzed the bias field free auto-oscillation in single-NC SHNOs with 100 nm and 150 nm constriction widths. Figure 2(a) shows the comparison of the current tunability of characteristic auto-oscillation frequency (the dominant first harmonic) for 100-nm single-NC SHNO (blue), 150-nm single-NC SHNO (red), and the NC pair (green). We observe that for lower value of I_{dc} (<1.45 mA) the auto-oscillation in the NC pair is purely driven by the auto-oscillation of 100-nm-wide NC (left NC). Therefore, the auto-oscillation frequency of the NC pair overlaps with the auto-oscillation frequency of 100-nm single-NC SHNO. However, at $I_{dc} \geqslant 1.45$ mA, the magnetization auto-oscillation takes place at the 150-nm-wide NC (right NC) as well. At this point both SHNOs couple with each other. Therefore, the auto-oscillation frequency of the NC pair deviates from the characteristic auto-oscillation frequencies of single-NC SHNOs. This coupling is identified as negative coupling [9,44] as the auto-oscillation frequency in mutually synchronized state is lower than the individual frequencies of single-NC SHNOs. However, above 2.2 mA, the auto-oscillation frequency at mutually synchronized state rapidly shifts towards higher frequency, as compared to the characteristic frequencies of single-NC SHNOs. This indicates a positive coupling [44] between the SHNOs at higher current.

It should be noted that the frequency of auto-oscillation in such anisotropy-assisted bias field free SHNO is primarily determined by the anisotropy field $\boldsymbol{H}_{\rm anis} = \frac{2K_u}{M_s}(\hat{\boldsymbol{u}} \cdot \boldsymbol{m})\hat{\boldsymbol{u}}$ as discussed in our previous report [33]. At higher input current, stronger SOT leads to increase in the amplitude of magnetization precession. Hence, $\boldsymbol{m}$ moves away from the easy axis (along $\hat{\boldsymbol{u}}$), resulting in a reduction of $\boldsymbol{H}_{\rm anis}$,which in turn reduces the auto-oscillation frequency. This explains the redshift behavior of the auto-oscillation frequency in such bias field free SHNOs. Therefore, the sudden blueshift at $I_{dc} > 2.2$ mA can be attributed to the reduction of auto-oscillation amplitude, which is also evident from the diminishing FFT amplitude in Fig. 1(d). This could be possible if there is a substantial phase difference between the local magnetization auto-oscillation at the NCs. Despite the high amplitudes of local magnetization auto-oscillation at the NCs at higher I_{dc}, this phase difference would lead to a reduction of the resultant oscillation amplitude of $\boldsymbol{m}$ in the NC pair. Hence, the NC pair exhibits a nonmonotonic frequency variation as a function of I_{dc} unlike the single NC SHNOs.

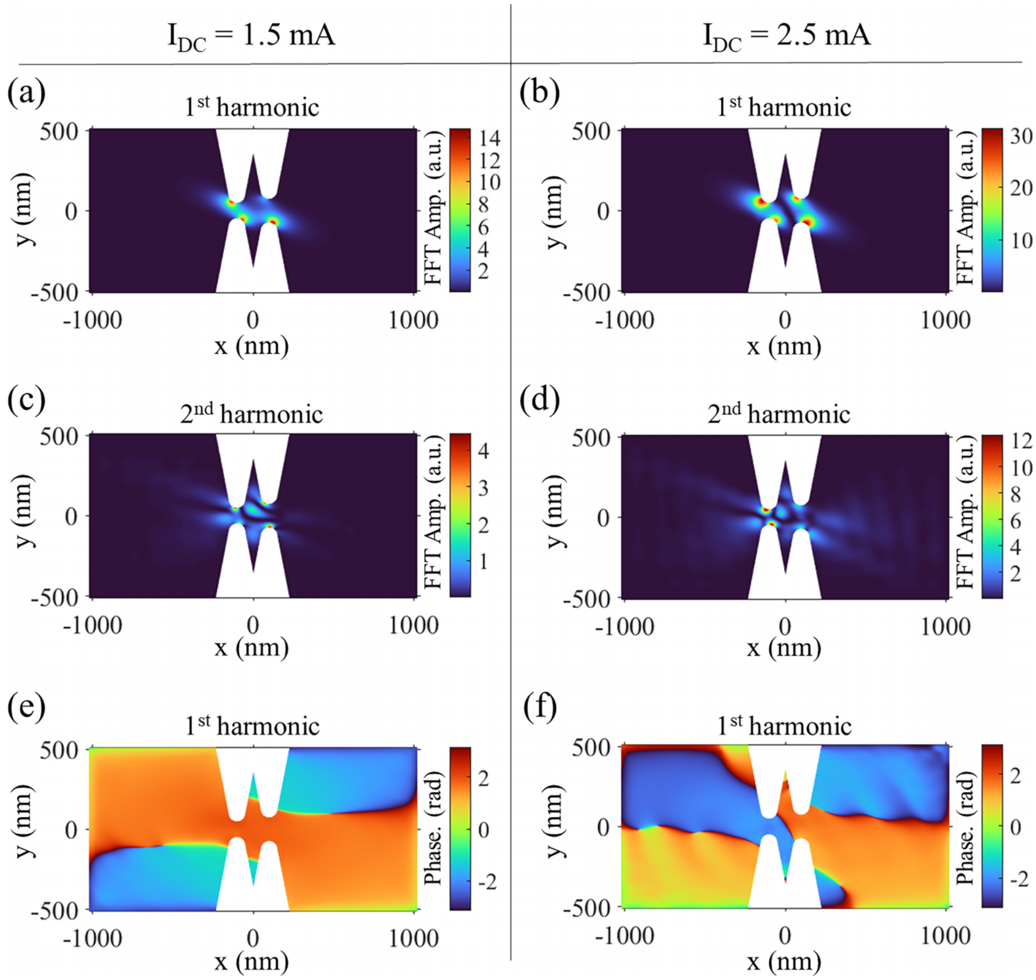

FIG. 3. Spatial profile of auto-oscillation amplitude and phase in the NC pair. The left colum shows a typical in-phase auto-oscillation (I_{dc} = 1.5 mA) and the right column shows a typical phase-binarized auto-oscillation state (I_{dc} = 2.5 mA). The spatial profiles of auto-oscillation amplitude have been shown for first harmonic in (a) and (b), and for second harmonic in (c) and (d). The spatial profiles of phase at the first harmonic are shown in (e) and (f).

B. Phase binarization in mutually synchronized state

Now we proceed to investigate the behavior of the phase difference (δ) for the first harmonic between the two SHNOs in the NC pair at mutually synchronized state. Figure 2(b) shows the behavior of δ as a function of I_{dc}. We notice that up to 2.2 mA, δ is quite small (within $\pi/9$ rad). That indicates both the NC SHNOs exhibit (nearly) in-phase auto-oscillation at this range of I_{dc}. In contrast, for $I_{dc} \geqslant 2.25$-mA current, δ becomes significant ($\delta \sim 8\pi/9$ rad), indicating (nearly) out-of-phase auto-oscillation in both NCs. Figure 2(c) shows the local $m_x(t)$ in both the NCs exhibiting in-phase auto-oscillation at $I_{dc} = 1.5$ mA and out-of-phase auto-oscillation at $I_{dc} = 2.5$ mA.

We observe that the NC pair exhibits two discrete auto-oscillation states in terms of phase difference (δ) between the local magnetization auto-oscillation at both NCs. In the out-of-phase auto-oscillation state, the discretization of individual phases of the two NCs to two distinctive phase states is known as the "phase binarization" [29,45]. Of course, the phase binarization observed in our NC pair is not exactly the ideal case, i.e., $\delta = \pi$. The reason will be explained later in this section. However, the phase difference between the individual NCs is large enough to classify the individual phases as *binarized*. Typically, the phase binarization in coupled oscillator system is realized through the SHIL method [45], where the oscillation frequency (f) of the system is "locked" by an external periodic signal (referred to as the "locking signal" later on) of frequency $2f$ [29]. We emphasize that the phase binarization in our NC pair has been achieved in the absence of any biasing magnetic field and external locking signal; therefore, it is purely driven by the input dc current.

To understand the underlying mechanism of phase binarization in the NC pair, we first look at the spatial profile of auto-oscillation amplitude. We look for the interaction between spin-wave modes, particularly in the vicinity of the constrictions. Figure 3 depicts these spatial profiles for an in-phase ($I_{dc} = 1.5$ mA) and a phase-binarized ($I_{dc} = 2.5$ mA) auto-oscillation states. In both cases, the first harmonics are localized spin-wave edge modes [19]. These edge modes overlap between the NCs for $I_{dc} = 1.5$ mA [Fig. 3(a)], reinforcing the in-phase synchronization of the local auto-oscillations in both NCs. On the other hand, the edge modes of the two NCs are discrete in space for $I_{dc} = 2.5$ mA [Fig. 3(b)] as

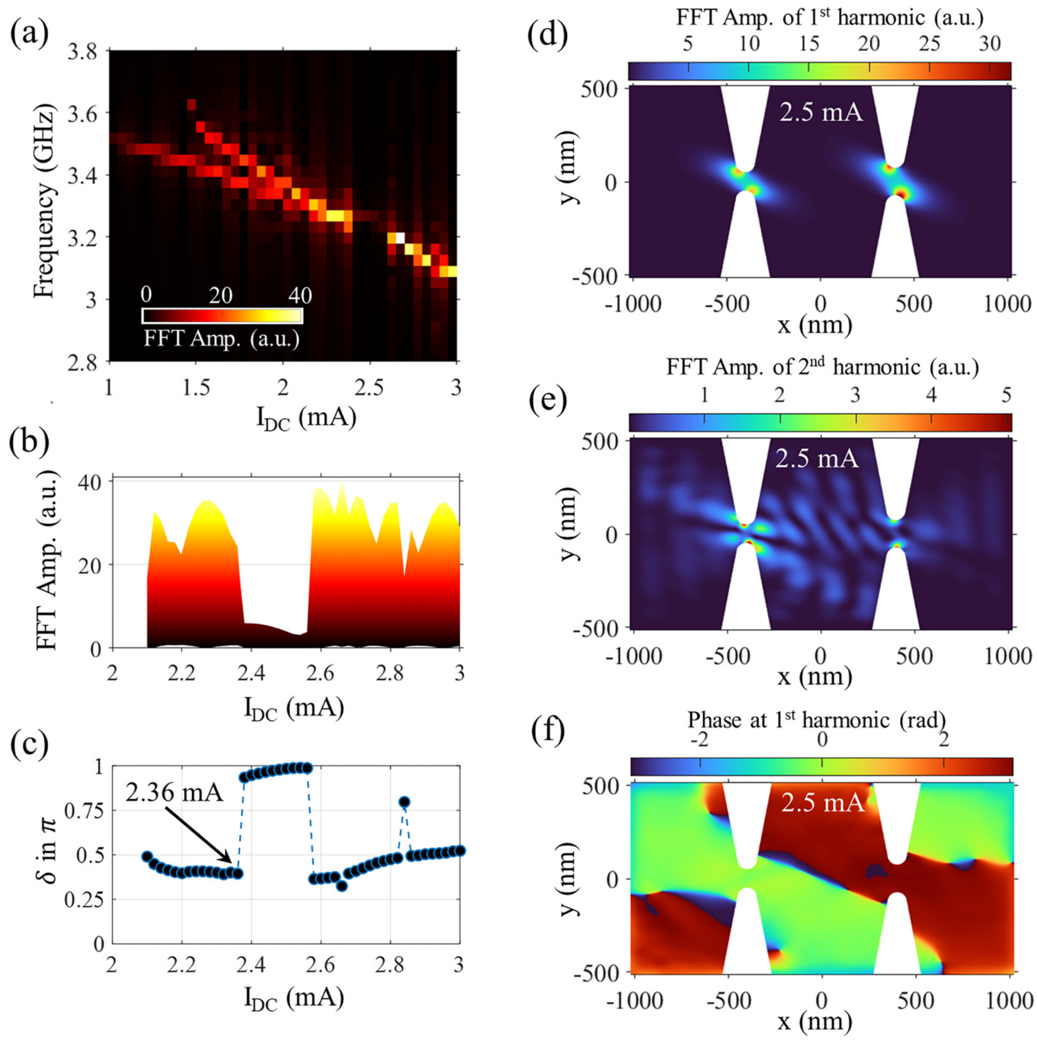

FIG. 4. Auto-oscillation characteristics in NC pair with $d = 800$ nm. (a) Current tunability of auto-oscillation frequency obtained from the entire NC pair geometry. (b) Variation of FFT amplitude as a function of I_{dc} in the mutually synchronized state. (c) Phase difference between the local auto-oscillation in the NCs. The phase binarization threshold current is denoted as 2.36 mA. (d), (e) Spatial profile of auto-oscillation amplitude at first and second harmonic, respectively, in phase-binarized state. (f) Spatial profile of phase of first harmonic at the phase-binarized state.

observed by the well-demarcated existence of nearly zero FFT amplitude region in between the two NCs. Therefore, in this case, the first harmonics (the dominant harmonics) of the auto-oscillation in both NCs hardly drive each other for in-phase synchronization. In contrast to the first harmonic, the second harmonic is a propagating spin-wave mode that creates the interference-like pattern in the spatial profile of auto-oscillation amplitude as seen in Figs. 3(c) and 3(d) (see Supplemental material [42], Fig. S2 as well). Hence, the phase binarization in the first harmonic is possibly being mediated by the second harmonic through SHIL mechanism, where one NC serves as the source of the *locking* periodic signal for the other NC. This is possible because of the characteristic frequency matching of the individual single-NC SHNOs at higher input current [see Fig. 2(a)].

We confirm the second-harmonic mediated phase binarization in our NC-pair SHNO by analyzing the magnetization auto-oscillation obtained from a similar NC pair with $d = 800$ nm. Figure 4 summarizes these results. In Fig. 4(a) we observe that the two NC SHNOs exhibit auto-oscillation at their free-running frequencies at lower currents, unlike the $d = 200$ nm NC pair. For $I_{dc} \sim 2.1$ mA onwards they mutually synchronize as their characteristic frequencies match in that range [see Figs. 4(a) and 1(a)]. The phase binarization [Fig. 4(c)] and its effect on auto-oscillation amplitude [Fig. 4(b)] have been clearly observed in the synchronized auto-oscillation state. Note that the out-of-phase state is quite close to the ideal case of phase binarization i.e., $\delta \sim \pi$ rad. However, the other phase state corresponding to $\delta \sim 2\pi/5$ rad is *weakly binarized*. The difficulty of in-phase synchronization is due to the longer separation between the NCs resulting in no overlapping of the localized edge modes as shown in Fig. 4(d). In contrast to the localized first harmonic, the second-harmonic spin-wave modes propagate from one NC to the other, resulting in generation of an interference-like pattern as shown in Fig. 4(e). Therefore, the propagating second harmonic reinforces the out-of-phase auto-oscillation [see the spatial phase map in Fig. 4(f)] through SHIL.

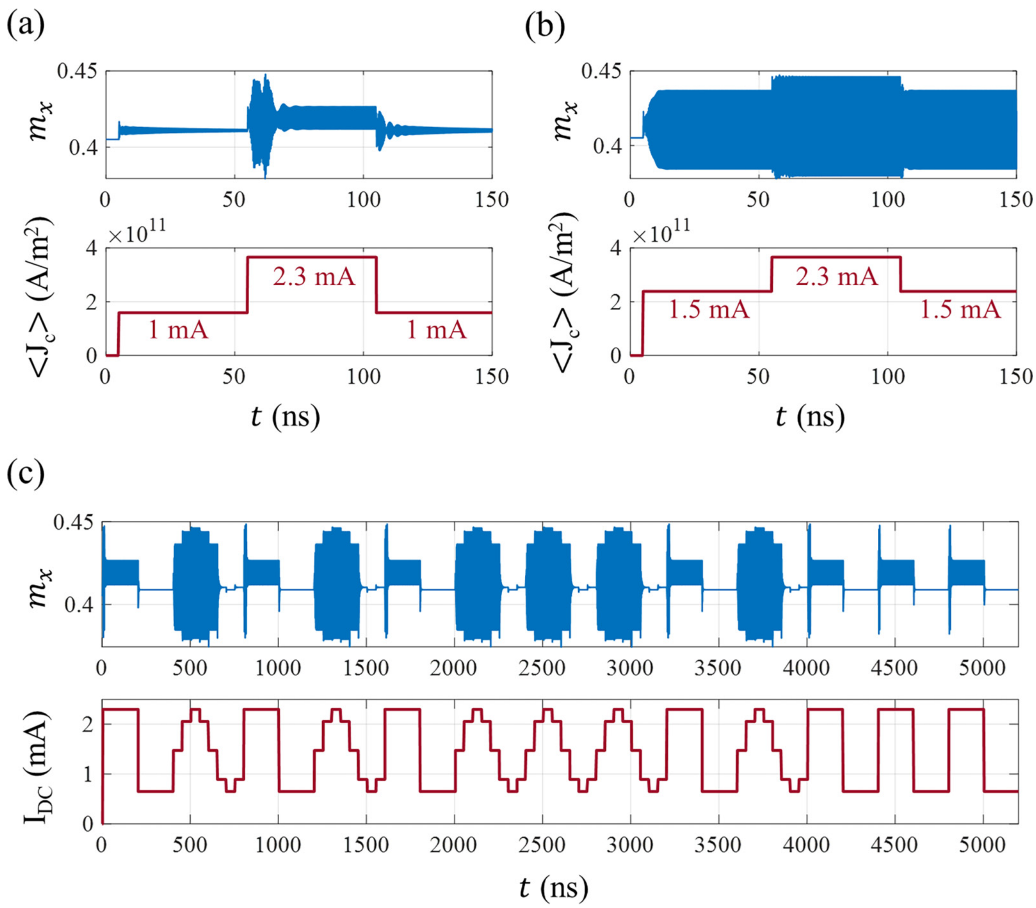

FIG. 5. Towards sin- and square-wave classification with phase-binarized NC pair. The time evolution of m_x in the NC SHNO pair ($d = 200$ nm) is shown for sequential excitation. (a) The time evolution of m_x (top subfigure) corresponding to the I_{dc} sequence 1 mA → 2.3 mA → 1 m A (bottom subfigure). The auto-oscillation amplitude at 2.3 mA reduces at the steady state due to phase binarization. (b) Time evolution of m_x for a slightly different I_{dc} sequence: 1.5 mA → 2.3 mA → 1.5 mA. Higher auto-oscillation amplitude at 2.3 mA at the steady state denotes in-phase auto-oscillation. The bottom subfigures in both (a) and (b) show the spatially averaged $\boldsymbol{J_c}$ as function of time. (c) Temporal profile of m_x for I_{dc} sequence defined by randomly arranged sin- and square waveforms.

We further note that the spin waves exhibit amplitude decay as they propagate due to the damping present in the ferromagnet. When the second-harmonic spin wave travels over 800 nm distance between the NCs, it experiences relatively higher decay in intensity as compared to the previous case of 200 nm separation between the NCs. Consequently, for identical input current, the SHIL-induced phase binarization takes place at higher threshold current. As seen from Fig. 2(b) and Fig. 4(c), the phase binarization threshold is 2.2 mA for $d = 200$ nm NC array, and 2.36 mA for $d = 800$ nm NC array.

Last, we would like to mention that the SHIL-induced phase binarization strongly depends on the power of the locking signal. SHIL-induced stable phase binarization in bias field assisted SHNO array is achieved above a certain threshold power of the locking signal. However, these SHNOs may switch between in-phase and out-of-phase auto-oscillation states below the threshold power of the locking microwave [29]. In the present bias field free SHNO pair, the intensity of the second harmonic is an order of magnitude smaller than the 1st harmonic. This intensity can only be enhanced by increasing the I_{dc}. However, change in I_{dc} leads to variation in the spatial profile of the spin-wave modes in the vicinity of the NCs (see Supplemental Material [42], Fig. S4), which may or may not favor the out-of-phase auto-oscillation [46]. Therefore, the phase binarization in our bias field free NC SHNO pair is current tunable, which is later utilized for implementation of RC scheme.

C. Reservoir computing with phase-binarized SHNO pair

We now demonstrate how the phase binarization can be utilized to perform efficient binary classification task using the NC SHNO pair as a reservoir. The learning task we choose is the classification of points that belong to randomly sequenced sin and square waveforms with identical period and amplitude. This is a standard RC benchmark task that requires significant nonlinearity as well as short-term memory. Notably, the points belonging to the extrema of sin- and square waves are completely identical; therefore, the classification of these points is not trivial. One must remember the previous points to classify the extrema points. It has been observed that the phase binarization in the NC pair strongly depends on the recent history of input current in a continuous sweep of I_{dc}. This has been demonstrated in Figs. 5(a) and 5(b). Here, we observe the auto-oscillation in the full NC pair geometry at 2.3 mA input current pulse, which follows an input current of

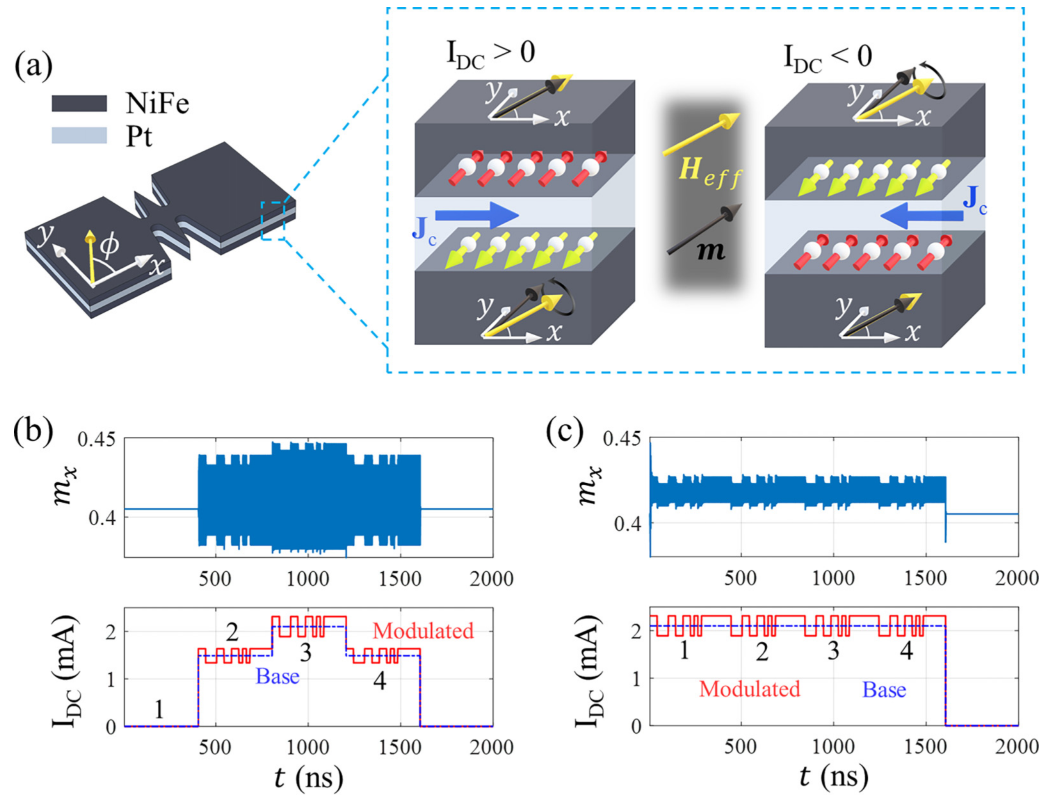

FIG. 6. Modified trilayer SHNO geometry for RC. (a) Schematic of the trilayer NC SHNO pair and the magnetization auto-oscillation under the change in polarity of I_{dc}. The yellow arrow in the trilayer NC SHNO pair geometry represents the easy axis that primarily decides the orintation of $\boldsymbol{H}_{\mathrm{eff}}$. (b), (c) Time evolution of m_x under the modulated I_{dc} representing the time-multiplexed inputs corresponding to the four consecutive points in the positive half of sin- and square waves, respectively. The "base" represents the I_{dc} values corresponding to the actual input data points. The time-multiplexed, i.e., preprocessed, input for the RC is represented by the "modulated" I_{dc}.

1 mA [Fig. 5(a)] and 1.5 mA [Fig. 5(b)] separately. We find that in the first case, phase binarization is achieved at 2.3 mA as expected, which results in the reduced auto-oscillation amplitude in steady state [Fig. 5(a)]. However, in stark contrast to the first case, the phase binarization is not achieved at 2.3 mA in the second case, which results in distinctively higher auto-oscillation amplitude in steady state [Fig. 5(b)]. Therefore, the phase binarization depends on the previous auto-oscillation state. The stable in-phase auto-oscillation state is reinforced by the spatial overlapping of the localized spin-wave edge modes corresponding to the stronger first harmonic. Therefore, it is difficult for the weaker second harmonic to induce phase binarization through SHIL. Hence, if the initial state is a steady in-phase auto-oscillation state, higher input current is required for phase binarization as compared to the stable initial state of $\boldsymbol{m}$. We utilize this phenomenon as a short-term memory feature where the auto-oscillation state associated with the "present" input ($I_{dc} = 2.3$ mA in Figs. 5(a) and 5(b)] is dictated by the "recent past" input [$I_{dc} = 1$ or 1.5 mA in Figs. 5(a) and 5(b)]. We further notice that the initial auto-oscillation state is restored once the input current is reduced back to 1 mA [Fig. 5(a)] or 1.5 mA [Fig. 5(b)], indicating the memory is not a long-term memory.

Now, we define a temporal sequence of randomly arranged sin and square waveforms of equal amplitude and period. Each waveform consists of eight points equally spaced in time. This input-time series is encoded in the magnitude of I_{dc} as shown in Fig. 5(c). For every single point in the time series, the associated I_{dc} is kept fixed for 50 ns to record the steady-state auto-oscillation profile. The time evolution of m_x obtained from a continuous simulation for the entire sequence of I_{dc} consisting of 104 input points (13 waveforms) is shown in Fig. 5(c). We clearly observe the substantial difference in the auto-oscillation profiles corresponding to the sin and square waveforms. The phase binarization takes place only for points belong to the square waveform, resulting in lower amplitude of $m_x(t)$. Therefore, the maxima points can be well classified despite the degeneracy in their values. However, the points in the lower half of the waveforms including the minima points do not produce any auto-oscillation as the I_{dc} is lower than the threshold excitation current [~ 1.1 mA for $p = 200$ nm as seen from Fig. 1(d)]. Therefore, these points cannot be classified using the present NC pair SHNO.

This issue could be resolved using the concept of a bipolar SHNO [47]. We add two similar NiFe layers with uniaxial anisotropy at both sides of the Pt layer [Fig. 6(a)]. In this modified structure, the auto-oscillation can be induced in either one of the NiFe layers by altering the polarity of I_{dc}. As shown in Fig. 6(a), the orientation of spin polarization and $\boldsymbol{m}$ in the bottom NiFe layer is such that the SOT opposes the damping torque. Hence, the bottom NiFe layer can exhibit auto-oscillation. On the other hand, in the top NiFe layer, the $\boldsymbol{m}$ and the spin-polarization direction are oriented such a way that the SOT and the damping torque act parallel to

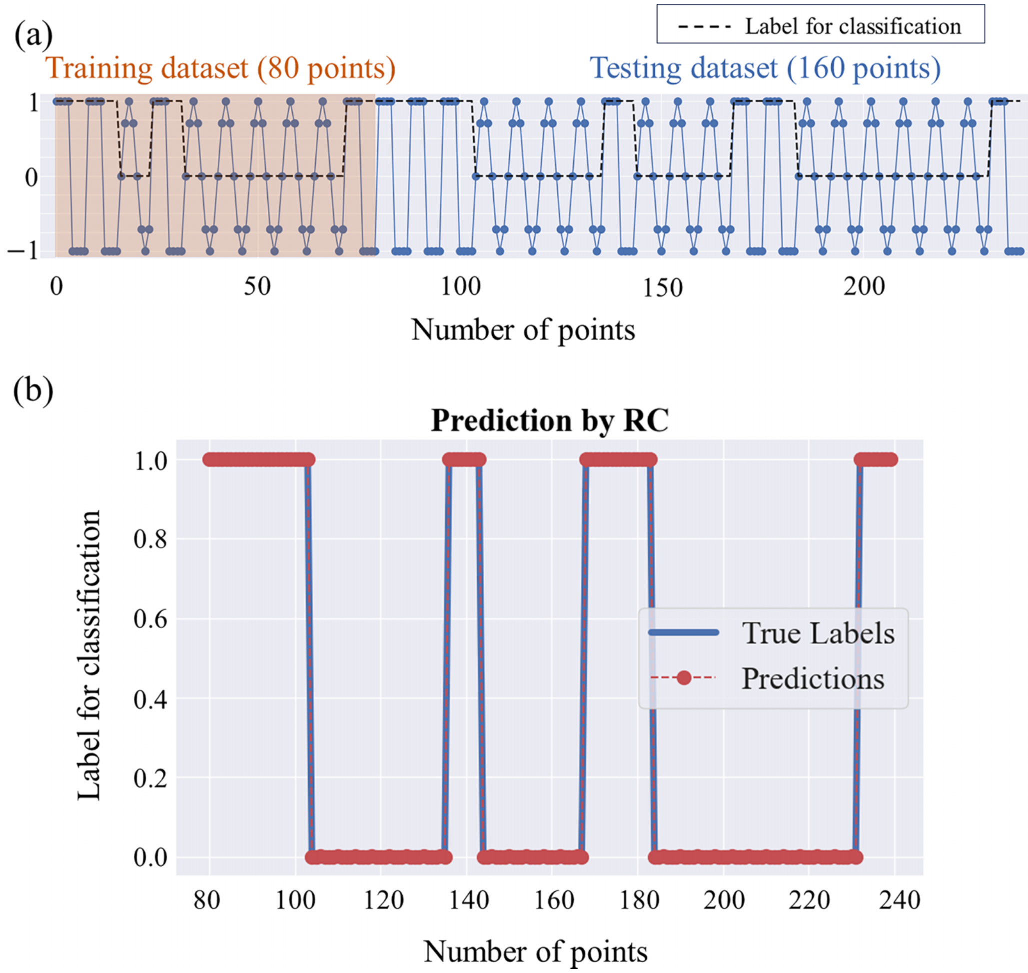

FIG. 7. Performance of trilayer NC SHNO pair in sin- and square-wave classification task. (a) The input points belonging to randomly sequenced sin- and square waveforms. First 80 points have been used for training the reservoir. The RC performance in the classification task has been tested with the remaining 160 data points. The binary labels assigned to the input points are shown in dashed line. (b) Comparison between the true classifier labels of the points and the prediction by the NC SHNO pair as a reservoir. The match between the true labels and the predicted labels shows 100% classification accuracy.

each other. This leads to an enhancement of the effective damping in the FM layer and eventually relaxation of $\boldsymbol{m}$ to a stable equilibrium state. The scenario reverses for $I_{dc} > 0$, where only the top NiFe layer can exhibit auto-oscillation of $\boldsymbol{m}$. Therefore, the auto-oscillation can be obtained in such a trilayer SHNO irrespective of the polarity of input current.

We now reconstruct the I_{dc} sequence in line with the main time series such that the amplitudes of the sin and square waves span symmetrically about $I_{dc} = 0$. In addition, we modulate the I_{dc} values through a standard time-multiplexing algorithm [48,49] (see Supplemental Material, note 5 for details [42]). The time multiplexing enables us to simulate multiple virtual neurons randomly connected to each other from a single dynamic node, which is the trilayer NC SHNO pair in our case. This essentially maps each point in the input to a higher-dimensional space as per the requirement of the reservoir in RC. Here, we simulate 20 virtual nodes (neurons). Therefore, each input point can be represented by the combined auto-oscillation state of all 20 nodes in the so-called higher-dimensional space.

Figures 6(b) and 6(c) show the auto-oscillation profile for the positive half cycles of sin- and square waveform, respectively, each consisting of four points. In Fig. 6(b), the constant "base" I_{dc} value representing a single point belonging to the sin waveform is shown in blue dashed-dotted line. The corresponding "modulated" I_{dc} values representing inputs for the virtual nodes are shown in continuous red line. Note that the oscillation amplitude fluctuates due to the modulation in I_{dc} values, showing the randomness in the system. Similar auto-oscillation data obtained for the points in the positive half of the square wave are shown in Fig. 6(c). We observe the noticeable difference in the auto-oscillation amplitude for sin- and square-wave points. The same auto-oscillation profiles have been obtained for the negative half of the waveforms due to auto-oscillation in the top NiFe layer. However, we still need to achieve a finite and relatively higher auto-oscillation amplitude for $I_{dc} = 0$ mA, to classify the zero-value points in the sin-wave category. This can be achieved by connecting an oscillator of comparable frequency and amplitude preceded by a NOT gate, in parallel to the NC pair (see Supplemental Material [42], Fig. S6).

Finally, to demonstrate the classification performance of our NC pair SHNO as a reservoir, we define the time series with 240 points (30 waveforms) as shown in Fig. 7(a). We use the first 80 points for training and the remaining 160 points for testing. We further define the binary target labels to the points: "1" for the points in square wave and "0" for the points in sin wave [the black dotted line in Fig. 7(a)]. Figure 7(b) shows the efficient prediction of the target labels by the reservoir which are 100% accurate with the true labels. The classification task has been performed with different random sequences of sin and square waves consisting of the same periodicity and number of points. A few of the results have been shown in the Supplemental Material [42], Fig. S7. Notably, in all these cases 100% accurate classification have been achieved.

III. CONCLUSION

We have demonstrated purely dc current-tunable mutual synchronization and phase binarization in an NC SHNO pair in the absence of biasing magnetic field as well as external microwave for injection locking. The coupling between the two nonidentical SHNOs is mainly mediated by the magnetodipolar interaction that leads to coherent synchronization of the SHNOs (see Supplementary Material, note 8 [42]). However, the characteristic frequencies of the single-NC SHNOs are tens of megahertz apart at lower input current. Therefore, mutual synchronization of such nonidentical SHNOs is apparently difficult to achieve at low current regime [$1.5\,\mathrm{mA} \leqslant I_{dc} \leqslant 1.75\,\mathrm{mA}$; see Fig. 2(a)]. Nevertheless, both the NC SHNOs in our NC pair with $d = 200$ nm exhibit mutually synchronized auto-oscillation state in this regime. This has been possible through the modulation of the local anisotropy field at the NCs by the overlapping of the localized spin-wave edge modes corresponding to the first harmonic. We recall that the local anisotropy field is directly determined by the instantaneous orientation of magnetization. The magnetodipolar coupling, as well as overlapping of the localized spin-wave edge modes, regulates the orientation of instantaneous magnetization and reinforces coherent auto-oscillation. This, in turn, modulates the local anisotropy field in such a way that leads to similar instantaneous auto-oscillation frequencies in both SHNOs in the NC pair. In contrast to $d = 200$ nm NC pair, there is no overlapping in the spin-wave mode profile of the first harmonic in $d = 800$ nm NC pair [Fig. 4(d)]. Therefore, in that case, both the NCs exhibit auto-oscillation at their characteristic frequencies in unsynchronized state for low input current [see Fig. 4(a)]. At higher values of input current, similar characteristic frequencies of both NC SHNOs lead to mutual synchronization for both $d = 200$ nm and $d = 800$ nm NC pairs [Figs. 1(d) and 4(a)]. In addition, we observe the phase binarization phenomena at mutually synchronized auto-oscillation state and its strong dependence on the recent history of dynamic magnetization. These phenomena have been utilized for performing an RC benchmark classification task as demonstrated in this paper. It should be noted that the RC scheme, demonstrated here, is not to contrast different algorithm and propose a better alternative, but to highlight the physical phenomena of dc current-driven phase binarization in realizing a simple RC network.

While all the simulation results presented here are obtained without considering any thermal effect to focus more on understanding the physical origin and impact of the observed phenomena as well as to reduce simulation time, the effect of finite temperature ($T = 300$ K) has been presented in the Supplemental Material [42] (Fig. S9). Similar phenomena of mutual synchronization and subsequent phase binarization have been observed for $T = 300$ K as well in the NC SHNO pair. Hence, our results hold promises to pave the way for overcoming challenges in synchronizing nonidentical bias field free NC SHNOs and utilize them for designing efficient RC hardware.

The data that support the findings of this study are available from the corresponding author upon reasonable request. The MUMAX3, PYTHON, and MATLAB codes used in this study are available from the corresponding author upon reasonable request [50].

ACKNOWLEDGMENTS

S.M. acknowledges the support from the NTU-Research Scholarship (NTU-RSS). R.S.R. acknowledges the support from the National Research Foundation (NRF), Singapore through Grant No. NRF-CRP21-2018-0003 and the Ministry of Education, Singapore, through its Academic Research Tier 1 Grant No. RG76/22.

S.M. conceived the original idea, performed all the micromagnetic simulations, did all the analysis of the simulation results, and drafted the manuscript; R.M., J.R.M., Y.F., and R.S.R. reviewed the manuscript and provided valuable inputs; and R.S.R. supervised the project.

The authors declare no competing interests.

Any opinions, findings, and conclusions or recommendations expressed in this material are those of the author(s) and do not reflect the views of the Ministry of Education, Singapore.

APPENDIX: DEVICE DESIGN AND MICROMAGNETIC SIMULATION METHODOLOGY

1. Device design in COMSOL

The NC SHNO pair has been designed considering a bilayer stack of 5-nm-thick NiFe layer interfaced with a 5-nm-thick Pt layer. Both the round-edged NCs in the NC pair have been defined with 50 nm radius of curvature and 22° opening angle. The widths of the left and right NCs are defined, respectively, as 100 and 150 nm [Fig. 1(a)]. The centers of both NCs are collinear and equally apart from the longer sides of the device. The geometry of this bilayer NC SHNO pair has been designed in COMSOL MULTIPHYSICS software. In addition, the spatial distribution of $\boldsymbol{J}_c$ in the Pt layer and the Oersted field in the NiFe layer corresponding to 1 mA input current (I_{dc}) have been simulated in COMSOL considering the standard conductivity values of 8.9 MS/m for Pt and 1.74 MS/m for NiFe.

2. Micromagnetic simulation

The micromagnetic simulations have been performed using the GPU-accelerated open-source software MUMAX3 [43] that employs a finite-difference discretization of space. A $2048\,\mathrm{nm} \times 1024\,\mathrm{nm} \times 5\,\mathrm{nm}$ simulation area has been uniformly discretized into 1024×512×1 rectangular grid. The relevant SHNO device geometry (NC pair or single-NC SHNOs) for micromagnetic simulation was extracted from COMSOL as a black and white image to define the NiFe region. MUMAX3 solves the LLG equation [Eq. (2)] in a ferromagnet. Therefore, only the NiFe layers of the SHNO devices have been simulated explicitly considering the Slonczewski-like spin-orbit torque term. The material parameters have been defined as follows [19,33]: $M_s = 600$ kA/m; exchange stiffness constant $A_{ex} = 10$ pJ/m; intrinsic damping parameter $\alpha = 0.02$; effective gyromagnetic ratio $\gamma/2\pi = 29.53$ GHz/T; and uniaxial magnetic anisotropy constant $K_u = 7.5$ kJ/m^3. To avoid the staircase effect at the circular edges of the NCs, the "edgesmooth" function of MUMAX3 has been used. Finally, absorbing boundary condition [51] has been implemented to avoid the spurious reflection of spin wave from the boundaries.

The SOT term has been implemented in MUMAX3 using the built-in Slonczewski spin-transfer torque (STT) model and disabling the Zhang-Li torque, following the approach of Dvornik *et al.* [19]. The distribution of current density and associated Oersted field are imported from the COMSOL simulation and adjusted for each value of the dc current. The spin-Hall angle of Pt has been defined as $\theta_{SH} = 0.08$ [19,24,25] and assigned to the variable "Pol" in the Slonczewski STT model in MUMAX3. The spin-polarization direction ($\boldsymbol{\sigma} = -\hat{\boldsymbol{y}}$) has been implemented by setting the "Fixedlayer = vector (0, −1, 0)" command. In addition, the "epsilonprime" variable in the Slonczewski STT model has been set to "0" to neglect the fieldlike component of SOT in our simulation. To simulate only SOT-driven magnetization dynamics, the initial magnetization has been relaxed into the ground state. Thereafter, a 5 ns initial delay has been introduced in the SOT to simulate the transient dynamics of magnetization in the absence of any SOT and Oersted field and finally relaxes to a stable magnetization state. For each value of I_{dc}, the simulation has been carried out for 70 ns and the $m_x(t)$ of the last 30 ns (steady-state auto-oscillation) has been analyzed. In case of $T = 300$ K, the simulation time has been fixed to 140 ns for each I_{dc} value, while the $m_x(t)$ obtained from last 40 ns has been analyzed. The postprocessing of the data has been done using custom-built MATLAB and PYTHON codes.

[1] G. Tanaka, T. Yamane, J. B. Héroux, R. Nakane, N. Kanazawa, S. Takeda, H. Numata, D. Nakano, and A. Hirose, Recent advances in physical reservoir computing: A review, Neural Netw. **115**, 100 (2019).

[2] H. Jaeger and H. Haas, Harnessing nonlinearity: Predicting chaotic systems and saving energy in wireless communication, Science **304**, 78 (2004).

[3] M. J. Marinella and S. Agarwal, Efficient reservoir computing with memristors, Nat. Electron. **2**, 437 (2019).

[4] J. Torrejon, M. Riou, F. A. Araujo, S. Tsunegi, G. Khalsa, D. Querlioz, P. Bortolotti, V. Cros, K. Yakushiji, A. Fukushima *et al.*, Neuromorphic computing with nanoscale spintronic oscillators, Nature (London) **547**, 428 (2017).

[5] B. Popescu, G. Csaba, D. Popescu, A. H. Fallahpour, P. Lugli, W. Porod, and M. Becherer, Simulation of coupled spin torque oscillators for pattern recognition, J. Appl. Phys. **124**, 152128 (2018).

[6] E. Goto, The parametron, a digital computing element which utilizes parametric oscillation, Proc. IRE **47**, 1304 (1959).

[7] I. Mahboob and H. Yamaguchi, Bit storage and bit flip operations in an electromechanical oscillator, Nat. Nanotechnol. **3**, 275 (2008).

[8] G. Csaba and W. Porod, Coupled oscillators for computing: A review and perspective, Appl. Phys. Rev. **7**, 011302 (2020).

[9] N. Garg, S. V. Hemadri Bhotla, P. K. Muduli, and D. Bhowmik, Kuramoto-model-based data classification using the synchronization dynamics of uniform-mode spin Hall nano-oscillators, Neuromorph. Comput. Eng. **1**, 024005 (2021).

[10] M. Zahedinejad, H. Mazraati, H. Fulara, J. Yue, S. Jiang, A. A. Awad, and J. Åkerman, CMOS compatible W/CoFeB/MgO spin Hall nano-oscillators with wide frequency tunability, Appl. Phys. Lett. **112**, 132404 (2018).

[11] A. Slavin and V. Tiberkevich, Nonlinear auto-oscillator theory of microwave generation by spin-polarized current, IEEE Trans. Magn. **45**, 1875 (2009).

[12] J. R. Mohan, A. J. Mathew, K. Nishimura, R. Feng, R. Medwal, S. Gupta, R. S. Rawat, and Y. Fukuma, Classification tasks using input driven nonlinear magnetization dynamics in spin Hall oscillator, Sci. Rep. **13**, 7909 (2023).

[13] H. Fulara, M. Zahedinejad, R. Khymyn, A. A. Awad, S. Muralidhar, M. Dvornik, and J. Åkerman, Spin-orbit torque–driven propagating spin waves, Sci. Adv. **5**, eaax8467 (2019).

[14] A. A. Awad, A. Houshang, M. Zahedinejad, R. Khymyn, and J. Åkerman, Width dependent auto-oscillating properties of constriction based spin Hall nano-oscillators, Appl. Phys. Lett. **116**, 232401 (2020).

[15] P. Dürrenfeld, A. A. Awad, A. Houshang, R. K. Dumas, and J. Åkerman, A 20 nm spin Hall nano-oscillator, Nanoscale **9**, 1285 (2017).

[16] V. E. Demidov, S. Urazhdin, A. Zholud, A. V. Sadovnikov, and S. O. Demokritov, Nanoconstriction-based spin-Hall nano-oscillator, Appl. Phys. Lett. **105**, 172410 (2014).

[17] J. Grollier, D. Querlioz, and M. D. Stiles, Spintronic nanodevices for bioinspired computing, Proc. IEEE **104**, 2024 (2016).

[18] M. Rajabali, R. Ovcharov, R. Khymyn, H. Fulara, A. Kumar, A. Litvinenko, M. Zahedinejad, A. Houshang, A. A. Awad, and J. Åkerman, Injection locking of linearlike and soliton spin-wave modes in nanoconstriction spin Hall nano-oscillators, Phys. Rev. Appl. **19**, 034070 (2023).

[19] M. Dvornik, A. A. Awad, and J. Åkerman, Origin of magnetization auto-oscillations in constriction-based spin Hall nano-oscillators, Phys. Rev. Appl. **9**, 014017 (2018).

[20] A. Kumar, M. Rajabali, V. H. González, M. Zahedinejad, A. Houshang, and J. Åkerman, Fabrication of voltage-gated spin Hall nano-oscillators, Nanoscale **14**, 1432 (2022).

[21] M. Zahedinejad, H. Fulara, R. Khymyn, A. Houshang, M. Dvornik, S. Fukami, S. Kanai, H. Ohno, and J. Åkerman, Memristive control of mutual spin Hall nano-oscillator synchronization for neuromorphic computing, Nat. Mater. **21**, 81 (2022).

[22] T. Hache, T. Weinhold, K. Schultheiss, J. Stigloher, F. Vilsmeier, C. Back, S. S. P. K. Arekapudi, O. Hellwig, J. Fassbender, and H. Schultheiss, Combined frequency and time domain measurements on injection-locked, constriction-based

spin Hall nano-oscillators, Appl. Phys. Lett. **114**, 102403 (2019).

[23] T. Hache, M. Vaňatka, L. Flajšman, T. Weinhold, T. Hula, O. Ciubotariu, M. Albrecht, B. Arkook, I. Barsukov, L. Fallarino *et al.*, Freestanding positionable microwave-antenna device for magneto-optical spectroscopy experiments, Phys. Rev. Appl. **13**, 054009 (2020).

[24] A. A. Awad, P. Dürrenfeld, A. Houshang, M. Dvornik, E. Iacocca, R. K. Dumas, and J. Åkerman, Long-range mutual synchronization of spin Hall nano-oscillators, Nat. Phys. **13**, 292 (2017).

[25] H. Mazraati, S. Muralidhar, S. R. Etesami, M. Zahedinejad, S. A. H. Banuazizi, S. Chung, A. A. Awad, R. Khymyn, M. Dvornik, and J. Åkerman, Mutual synchronization of constriction-based spin Hall nano-oscillators in weak in-plane magnetic fields, Phys. Rev. Appl. **18**, 014026 (2022).

[26] T. Kendziorczyk and T. Kuhn, Mutual synchronization of nanoconstriction-based spin Hall nano-oscillators through evanescent and propagating spin waves, Phys. Rev. B **93**, 134413 (2016).

[27] A. Kumar, H. Fulara, R. Khymyn, A. Litvinenko, M. Zahedinejad, M. Rajabali, X. Zhao, N. Behera, A. Houshang, A. A. Awad *et al.*, Robust mutual synchronization in long spin Hall nano-oscillator chains, Nano Lett. **23**, 6720 (2023).

[28] M. Zahedinejad, A. A. Awad, S. Muralidhar, R. Khymyn, H. Fulara, H. Mazraati, M. Dvornik, and J. Åkerman, Two-dimensional mutually synchronized spin Hall nano-oscillator arrays for neuromorphic computing, Nat. Nanotechnol. **15**, 47 (2020).

[29] A. Houshang, M. Zahedinejad, S. Muralidhar, J. Chęciński, R. Khymyn, M. Rajabali, H. Fulara, A. A. Awad, M. Dvornik, and J. Åkerman, Phase-binarized spin Hall nano-oscillator arrays: Towards spin Hall Ising machines, Phys. Rev. Appl. **17**, 014003 (2022).

[30] T. Shirokura and P. N. Hai, Bias-field-free spin Hall nano-oscillators with an out-of-plane precession mode, J. Appl. Phys. **127**, 103904 (2020).

[31] S. Manna, R. Medwal, and R. S. Rawat, Reconfigurable neural spiking in bias field free spin Hall nano-oscillator, Phys. Rev. B **108**, 184411 (2023).

[32] T. Taniguchi, Out-of-plane magnetization oscillation in spin Hall device assisted by field-like torque, Appl. Phys. Lett. **118**, 142406 (2021).

[33] S. Manna, R. Medwal, S. Gupta, J. R. Mohan, Y. Fukuma, and R. S. Rawat, Anisotropy-assisted bias-free spin Hall nano-oscillator, Appl. Phys. Lett. **122**, 072401 (2023).

[34] D. Marković, M. W. Daniels, P. Sethi, A. D. Kent, M. D. Stiles, and J. Grollier, Easy-plane spin Hall nano-oscillators as spiking neurons for neuromorphic computing, Phys. Rev. B **105**, 014411 (2022).

[35] M. Ito, S. Ono, H. Fukui, K. Kogirima, N. Maki, T. Hikage, T. Kato, T. Ohkochi, A. Yamaguchi, M. Shima *et al.*, Uniaxial in-plane magnetic anisotropy mechanism in Ni, Fe, and Ni-Fe alloy films deposited on single crystal Y-Cut 128° $LiNbO_3$ using magnetron sputtering, J. Magn. Magn. Mater. **564**, 170177 (2022).

[36] E. B. Park, Y.-C. Kim, S.-U. Jang, J.-H. Kim, S.-W. Han, and S.-J. Kwon, Induced magnetic anisotropy in permalloy films annealed with magnetic field, Met. Mater. Int. **19**, 129 (2013).

[37] R. Medwal, S. Gupta, R. S. Rawat, A. Subramanian, and Y. Fukuma, Spin pumping in asymmetric $Fe_{50}Pt_{50}/Cu/Fe_{20}Ni_{80}$ trilayer structure, Phys. Rapid Res. Lett. **13**, 1900267 (2019).

[38] K. Takanashi, M. Mizuguchi, T. Kojima, and T. Tashiro, Fabrication and characterization of $L1_0$-Ordered FeNi thin films, J. Phys. D: Appl. Phys. **50**, 483002 (2017).

[39] L. Liu, O. J. Lee, T. J. Gudmundsen, D. C. Ralph, and R. A. Buhrman, Current-induced switching of perpendicularly magnetized magnetic layers using spin torque from the spin Hall effect, Phys. Rev. Lett. **109**, 096602 (2012).

[40] L. Liu, T. Moriyama, D. C. Ralph, and R. A. Buhrman, Spin-torque ferromagnetic resonance induced by the spin Hall effect, Phys. Rev. Lett. **106**, 036601 (2011).

[41] T. Nan, S. Emori, C. T. Boone, X. Wang, T. M. Oxholm, J. G. Jones, B. M. Howe, G. J. Brown, and N. X. Sun, Comparison of spin-orbit torques and spin pumping across NiFe/Pt and NiFe/Cu/Pt interfaces, Phys. Rev. B **91**, 214416 (2015).

[42] See Supplemental Material at http://link.aps.org/supplemental/10.1103/PhysRevB.109.214425 for additional details. These include comparison of spatial profiles of the three components of current density vector, phase profile of the second harmonic spin wave, phase binarization for different values of anisotropy constant, role of magnetodipolar coupling in mutual synchronization and phase binarization at room temperature (300 K). In addition, a schematic of the proposed circuit using the trilayer SHNO and NOT gate, the detailed description of preprocessing of input data using the time multiplexing method for the reservoir computing task and the classification performance for six different random sequences of sin and square waves are presented in the Supplemental Material.

[43] A. Vansteenkiste, J. Leliaert, M. Dvornik, M. Helsen, F. Garcia-Sanchez, and B. Van Waeyenberge, The design and verification of MuMax3, AIP Adv. **4**, 107133 (2014).

[44] E. M. Izhikevich, Computing with oscillators, Neural Networks **5255**, 1 (2000).

[45] A. Neogy and J. Roychowdhury, Analysis and design of sub-harmonically injection locked oscillators, in *Proceedings of the 2012 Design, Automation & Test in Europe Conference & Exhibition (DATE)* (IEEE, Piscataway, NJ, 2012), pp. 1209–1214.

[46] A. Kumar, A. kumar Chaurasiya, V. H. González, N. Behera, R. Khymyn, A. A. Awad, and J. Åkerman, Spin wave-driven variable-phase mutual synchronization in spin Hall nano-oscillators, arXiv:2402.00586.

[47] T. Hache, Y. Li, T. Weinhold, B. Scheumann, F. J. T. Gonçalves, O. Hellwig, J. Fassbender, and H. Schultheiss, Bipolar spin Hall nano-oscillators, Appl. Phys. Lett. **116**, 192405 (2020).

[48] D. Markovic, N. Leroux, M. Riou, F. A. Araujo, J. Torrejon, D. Querlioz, A. Fukushima, S. Yuasa, J. Trastoy, P. Bortolotti, and J. Grollier, Reservoir computing with the frequency, phase, and amplitude of spin-torque nano-oscillators, Appl. Phys. Lett. **114**, 012409 (2019).

[49] L. Millet, H. Jeon, B. Kim, B. Bhoi, and S.-K. Kim, Reservoir computing using photon-magnon coupling, Appl. Phys. Lett. **119**, 182405 (2021).

[50] MUMAX3, PYTHON, and MATLAB.

[51] G. Venkat, H. Fangohr, and A. Prabhakar, Absorbing boundary layers for spin wave micromagnetics, J. Magn. Magn. Mater. **450**, 34 (2018).